

The Link Between Packing Morphology and the Distribution of Contact Forces and Stresses in Packings of Highly Non-Convex Particles

N. A. Conzelmann^{1,2}, A. Penn¹, M. N. Partl², F. J. Clemens², L. D. Poulikakos², C. R. Müller¹

¹ ETH Zürich, Laboratory of Energy Science and Engineering, Department of Mechanical and Process Engineering, Institute of Energy and Process Engineering, Leonhardstrasse 21, 8092 Zürich, Switzerland

² Empa – Swiss Federal Laboratories for Materials Science and Technology, Überlandstrasse 129, 8600 Dübendorf, Switzerland

Keywords: Packing, Particle Shape, Non-Convex, Force Distribution, Force Chains, Morphology

ABSTRACT – An external load on a particle packing is distributed internally through a heterogeneous network of particle contacts. This contact force distribution determines the stability of the particle packing and the resulting structure. Here, we investigate the homogeneity of the contact force distribution in packings of highly non-convex particles both in two-dimensional (2D) and three-dimensional (3D) packings. A newly developed discrete element method (DEM) is used to model packings of non-convex particles of varying sphericity. The results show, that in 3D packings, the contact forces distribution becomes increasingly heterogeneous with decreasing particle sphericity. However, in 2D packings the contact force distribution is independent of particle sphericity, indicating that results obtained in 2D packings cannot be extrapolated readily to 3D packings. Radial distribution functions (RDFs) show that the crystallinity in 3D packings decreases with decreasing particle sphericity. We link the decreasing homogeneity of the contact force distributions to the decreasing crystallinity of 3D packings.

Introduction

Densely packed granular materials are frequently encountered in every-day life, for example, in civil engineering applications such as railway track ballast or porous asphalt pavements [1,2]. Such packings often undergo compaction either by forced compression or due to the material's own weight [3,4]. It has been well established that internal forces in packed granular materials are not distributed homogeneously [5,6], but instead, forces are transmitted within the material through a network of so-called force chains. This force chain network traverses through the whole particle packing, but transmits forces through only a subset of the packed particles that are subject to above-average loads [7,8]. When exceeding a critical stress value in a force chain, buckling and/or slipping events can occur which result in large scale rearrangements of the packing [9,10]. Hence, the topology of the force chain network affects critically the structural stability of the packing [11].

Studies on force chains can be largely categorized into studies that consider (i) 2D packings [6,7], i.e. packings comprised of only one particle layer, or 3D packings [5,12] and (ii) packings that are compressed or sheared [6,7,12]. Compressed packings are obtained either by the uniaxial

compression of particles in a rigid-walled container via a moving piston [12,13], or by its isotropic compression via two perpendicular wall [6,14]. To shear stress packings, various methods are used. For example placing particles in a rectangular confinement and compressing in one direction while expanding another direction [6]. Numerically, packings may be sheared by compressing the packing vertically, while introducing a constant horizontal velocity to a frictional top wall and allowing a free horizontal movement of the particles [14,15].

In 2D packings, force chains were first qualitatively and later quantitatively probed by transmitting polarized light through a sheared packing of photoelastic discs, visualizing the stress in the discs in the form of fringes [7,16]. This method was extended by Liu et al. [5] to 3D packings by immersing photoelastic beads in a liquid with a matching refractive index. It was found that the magnitude of the contact forces is distributed heterogeneously through the packing. To this date, there is no agreement on how to quantify force chains, but commonly the distribution of contact forces is quantified by the probability distributions of the contact forces [5,12,17]. For example, Liu et al. [5] placed carbon paper onto the inner surfaces of a container holding a particle packing. By calibrating the size of the imprints on the carbon paper against a known force they obtained the probability distribution ($P(f)$ with $f = F_n / \langle F_n \rangle$) of the normal contact forces (F_n) normalized by the mean normal contact force ($\langle F_n \rangle$). It was found that the probability of finding large normalized forces (i.e. $f > 1$) decays exponentially with increasing force magnitude. To explain this experimental observation, a theoretical model was proposed that assumes that the dominant mechanism which gives rise to force chains is governed by the heterogeneity of the granular packing, causing in turn, an unequal force distribution on the individual particles. It was observed further that $P(f)$ has a peak at $f = 1$ and that $P(f) \rightarrow 0$ for $f \rightarrow 0$. The shape of the observed probability distribution function of the contact forces resembles a characteristic shape commonly observed for disc- and sphere-shaped particles [5,12,13,15,17]. This characteristic shape is shown schematically in Figure 1 and labelled as type A, while the characteristic distribution labelled type B is, for example, observed in sheared packings of non-spherical particles [14,15]. A shortcoming of the carbon paper method is the difficulty to distinguish between beads that do not transmit a force and voids. This aspect was studied further by Mueth et al. [12] determining the fraction of contacts in compressed 3D packings that transmit forces that are sufficiently low to not leave an imprint on the carbon paper. Incorporating this additional information, Mueth et al. [12] found that $P(f)$ has a saddle point at $f = 1$ and $P(f)$ increases for $f \rightarrow 0$ instead of approaching zero as proposed by Liu et al. [5]. Hence, for $f > 0.5$ the $P(f)$ as observed by Mueth et al. [12] has a concave shape that is characteristic of a distribution of type A, but combined with an increasing probability for $f \rightarrow 0$, that is characteristic for a type B distribution (Figure 1). The previous observation of Liu et al. [5] that $P(f)$ decays exponentially for $f > 1$ was confirmed by Mueth et al. [12], who fitted the decaying part of $P(f)$, i.e. the region $f > 1$, by $P(f) \propto e^{-kf}$ where $k = 1.5$. More recently, Majmudar and Behringer [6] further improved the quantification of the magnitude of contact forces by using photoelastic discs and acquiring high-resolution photographs of 2D packings, allowing them to distinguish the individual interference fringes in the discs. Solving an inverse problem, which relates the number of fringes observed in a disk to the magnitude of the contact forces, the normal and tangential contact forces at each contact point were determined. Using this improved experimental technique, it was observed that in sheared packings fewer particles transmit large forces compared to compressed packings leading to more distinct force chains. Furthermore, it was shown that $P(f)$ in sheared and compressed packings of discs resembles a type A distribution with a peak at $f \approx 1$. However the coefficient k of the exponential decay is smaller for sheared packings when compared to compressed packings.

Despite the continuous development and improvement of experimental techniques to visualize and quantify contact forces, it remains challenging to extract quantitative information of contact forces, in particular in 3D packings that are of high practical relevance. To address these challenges, the discrete element method (DEM) has established itself as an alternative to experimental approaches [18],

providing detailed information on force networks in granular systems [19]. For example, Luding [17] used the DEM to investigate how the spatial stress distribution changes if polydispersity is introduced into packings of discs organized in a perfectly hexagonal lattice. For exactly monodisperse particle packings, particle stresses are distributed uniformly, in agreement with the hypothesis of Liu et al. [5]. However, as soon as polydispersity is introduced by varying the diameter (as little as $\pm 0.33\%$ of the mean diameter) a heterogeneous stress distribution, i.e. the occurrence of force chains was observed [17]. So far, most works on contact forces have been limited to spherical particle packings [5,6,8,12].

Among non-spherical particle packings studied, those composed of highly non-convex particles are particularly interesting as non-convex particles can interlock, forming packings that may sustain compressive and tensile forces despite containing purely non-cohesive particles [13,20]. Owing to these particular characteristics, packings of highly non-convex, interlocking particles may find practical relevance, for example in architecture by enabling novel construction concepts such as aleatory construction [21–24]. However, despite their intriguing characteristics, so far, only a few studies have investigated the distribution of contact forces, $P(f)$, in packings composed of non-spherical particles. For example, Gan et al. [25] performed 3D DEM simulations of packings of oblate ellipsoids with their sphericity (ψ) varying between 1 to 0.7. Interestingly, the $P(f)$ for ellipsoids was similar to the distribution of spheres, i.e. $P(f)$ peaks close to $f = 1$ and for $f > 1$ $P(f)$ decays exponentially (type A distribution). The exponential decay was fitted by $P(f) = e^{-kf}$ with k ranging between 1.2 and 1.4 depending on particle sphericity. However, there did not seem to be a clear correlation between the sphericity of the particles and the exponent k characterizing the decay. Similar results were reported by Saint-Cyr et al. [14] who simulated compressed packings of particle clusters composed of three discs glued together in a triangular arrangement (trimers). The sphericity of the trimer particles was varied between 1 and 0.76 by varying the overlap of the trimer particles. A key finding of their work was that in compressed packings of trimers, $P(f)$ resembles the distribution of spheres (type A) with an exponential decay $P(f) = e^{-kf}$ (for $f > 1$) with $k = 1.7$, independent of the particle sphericity, hence confirming the results of Gan et al. [25]. When the compressed trimer particles were also sheared (instead of only compressed), k decreased with decreasing sphericity (ψ), i.e. k reduces from 1.7 to 1 for ψ decreasing from 1 to 0.76. The behaviour of the reference case (discs with $\psi = 1$) was different in that $P(f)$ was not affected by the addition of shear. Furthermore, Saint-Cyr et al. [14] showed that in sheared packings of spheres, the shape of $P(f)$ is concave and resembles a type A distribution. However, for non-spherical particles with $\psi < 0.96$, $P(f)$ increases for $f \rightarrow 0$ leading to a type B distribution without a peak. Further, it was found that $\lim_{f \rightarrow 0} P(f)$ increased with decreasing sphericity.

The decreasing value of k for decreasing particle sphericity and the absence of a peak at $f \approx 1$ leads to the key conclusion that in sheared packings $P(f)$ becomes increasingly heterogeneous for decreasing sphericity. The results of Saint-Cyr et al. were confirmed by Azéma and Radjai [15] in 2D simulations of sheared, half-disc-capped rectangular particles which resemble 2D spherocylinders. Azéma and Radjai [15] varied the sphericity of the particles from 1 to 0.82 and found the exponent k in $P(f) = e^{-kf}$ to decrease from 1.8 to 0.85, respectively. Moreover, they could also confirm that for particles with $\psi < 0.99$ $P(f)$ resembles a type B distribution where $\lim_{f \rightarrow 0} P(f)$ increased for decreasing ψ . Highly non-convex particles of very low sphericity ($\psi = 0.45$) (and spheres as a reference case) were studied by Murphy et al. [13]. The objective of their work was to find particle shapes that can form free-standing, externally unconfined, packings that can support load (i.e. searching for packings of interlocking particles that can sustain compressive and tensile stresses). Particles of low sphericity were modeled by gluing together multiple spheres to yield Z-shaped particles. For the reference case, a 3D compressed packing of spheres, the well-established type A contact force distribution was observed, with a decay exponent of $k = 1.4$. However, compressed 3D packings of Z-shaped particles have a force distribution of type B, similar to the distributions observed by Saint-Cyr et al. [14] and Azéma and

Radjai [15] in 2D sheared packings of non-spherical particles ($0.96 > \psi > 0.76$). Additionally, the contact force distribution of Z-shaped particles ($\psi = 0.45$) had a very long exponential tail with an exponent k ranging between 0.56 and 0.76 depending on the specific Z-shape.

From the above we can conclude that in 2D packings the exponential tail of the contact force distribution, $P(f)$, becomes longer with increasing particle non-sphericity, i.e. k decreases with decreasing ψ . In addition the shape of $P(f)$ transitions from type A shape to a type B upon shearing [14,15]. However, in compressed 2D packings a decrease of k , as well as a change from a type A to type B distribution, with increasing particle non-sphericity does not occur for particles with $\psi > 0.76$. Conversely, in compressed 3D packings of particles with $\psi = 0.45$ a type B force distribution with $k \leq 0.76$ was observed. Hence, it remains still unclear whether (i) contact force distributions of type A prevail in compressed 2D packings of particles of low sphericity ($\psi < 0.76$) and (ii) the contact force distribution of low sphericity particles ($\psi < 0.76$) changes from a type A to type B distribution when transitioning from 2D to 3D packings.

In this work we aim to address these two questions utilizing the DEM to simulate compressed 2D and 3D packings of particles with a wide range of ψ values. In addition, we compute the radial distribution function (RDF) of particle packings to assess their morphology. Calculating the RDF allows us to probe whether the conclusion drawn by Liu et al. [5] and Luding [17] for spherical particles, viz. that a more heterogeneous packing morphology leads to a longer exponential tail, can be extended to non-spherical particles.

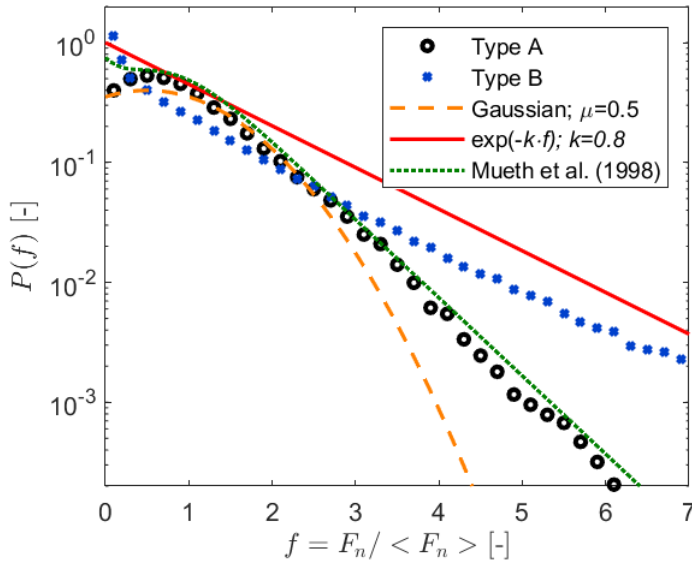


Figure 1: Probability distributions of f , i.e. the normal contact force (F_n) normalized by the mean normal contact force ($\langle F_n \rangle$). Distributions of type A and B represent characteristic shapes that have been observed in various particle packings. The type A and type B distributions were obtained for 3D packings studied in this work. Specifically, a type A distribution was obtained for spheres and a type B distribution for star-shaped particles with a sphericity (ψ) equal to 0.419.

Methods

The DEM algorithm used in this study is a modification of the original concept proposed by Cundall and Strack which was developed for disc-shaped particles [19]. The present work considers particles that have been created by combining multiple spherocylinders (cylinders with hemispherically capped ends), analogous to the commonly applied glued-sphere approach [26]. A spherocylinder is a computationally benevolent particle shape since all points on its surface have the same distance from the central axis (see Figure 2). The general concept used in the DEM to track particles and particle

contacts has been well documented in the literature [19,26–31]. Hence, the following will only describe the contact model and the contact detection algorithm between spherocylinders.

Particle contacts

Since all points on the surface of a spherocylinder have the same distance from the central axis (red dashed line in Figure 2), the contact detection for spherocylinders can be reduced to the task of finding the closest points between two line segments. We solve this task using the algorithm proposed by Lumelsky [32]. The point at which the contact forces act is the center point (green point in Figure 2) of the line that connects the two closest points on each of the central axes (blue line in Figure 2). If the angle between the central axes of the two contacting spherocylinders is less than two degrees, the contact is treated as a parallel contact (Figure 2b). The value of 2° was chosen as a feasible and efficient cut-off value based on preliminary experiments in the scope of this work. These experiments demonstrated that varying the cut-off angle between 0.01° and 5° does not affect the packing density nor the particle orientations. For a parallel contact, the middle of the parallel sections that align is chosen as the contact point (Figure 2b).

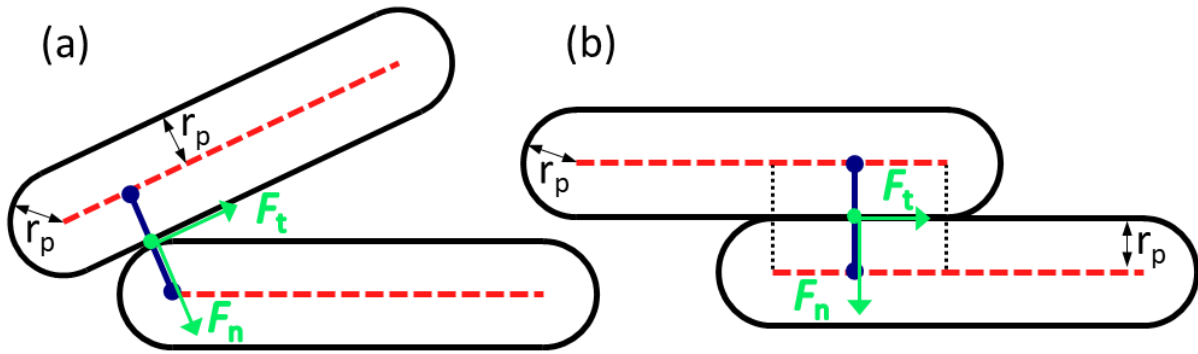


Figure 2: Schematic of two contacting spherocylinders. The red dashed lines denote the central axis of each spherocylinder. The spherocylinder radius is labelled r_p . The blue line depicts the shortest distance between the central axis of the two spherocylinders. F_n and F_t depict the normal and tangential forces acting at the contact point (green): a) contact between a cylindrical section and a hemispherical end cap, b) parallel contact between spherocylinders.

The contact between two particles is modeled by a spring-dashpot. In the normal direction (subscript n), the contact force F_n between the two contacting particles i and j is:

$$F_n = \max\left(0, \quad k_{nij}\delta_n - 2\eta_n\sqrt{m_{ij}k_{nij}v_n}\right) \quad (1)$$

The stiffness $k_{nij} = (k_{ni} * k_{nj}) / (k_{ni} + k_{nj})$ is calculated from the individual stiffnesses (k_{ni}, k_{nj}) of the contacting particles and δ_n is the overlap between the contacting particles. The damping factor in the normal direction η_n is assumed to be constant and v_n is the normal component of the relative velocity between the two particles at the point of contact. The effective inertial mass m_{ij} is calculated by:

$$m_{ij} = \frac{m_i * m_j}{m_i + m_j} \quad (2)$$

In the tangential direction (subscript t), the maximal contact force is limited by Coulomb's law of friction and is calculated by:

$$F_t = \min\left(\mu k_{nij}\delta_n, \quad k_{tij}\delta_t - 2\eta_t\sqrt{m_{ij}k_{tij}v_t}\right) \quad (3)$$

where μ is the coefficient of friction, η_t is the tangential damping factor and v_t is the tangential component of the relative velocity between the particles at the point of contact. The tangential stiffness k_{tij} is calculated analogously to the normal stiffness. The accumulated tangential displacement at the contact is calculated as $\delta_t = \int v_t dt$.

Table 1 summarizes the values of the parameters used in the simulations. The value of the parameters of the confining walls are identical to those of the particles, except for the friction coefficient, which was set to zero, minimizing the influence of the walls on the structure of the packings. Setting the friction coefficient to zero will aid the comparison with results that have been obtained from different packing configurations [33].

It has been argued that the material stiffness should increase with increasing contact area, e.g. in the case of a parallel contact between two spherocylinders (Figure 2b) [34–36]. However, a recent study has shown that varying the contact stiffness in the case of parallel contacts has little influence on the force distribution and structure in packings of spherocylinders [37]. Consequently, in this work, the normal and tangential stiffness were assumed to be constant, regardless of the geometry of the contact.

Table 1: Material parameters used in the simulations

Parameter	Symbol	Value
Normal stiffness	k_n	100000 N/m
Tangential stiffness	k_t	50000 N/m
Normal damping factor	η_n	0.2
Tangential damping factor	η_t	0.2
Coefficient of friction	μ	0.5
Spherocylinder diameter	d_p	0.005 m

Cluster particles

The combination of several spherocylinders to spherocylinder-cluster particles, analogous to the glued sphere approach [26,35], does not require additional contact detection routines [26]. The contact between two cluster particles can be treated as a contact between individual spherocylinders. The contact forces acting on the different spherocylinders belonging to a cluster are summed up and act on the center of gravity of the cluster.

In this study, two different types of cluster particles were investigated. In 2D packings, cross-shaped particles were used (Figure 3a-e). Cross-shaped particles are formed by intersecting two perpendicular spherocylinders of equal length in their centers. In simulations of pseudo-2D and 3D packings, star-shaped particles (also referred to as jacks or hexapods) were used. Such particles are formed by intersecting a cross-shaped particle with a third spherocylinder (of the same length) perpendicular to both spherocylinders that form the cross (Figure 3f). These particle shapes were chosen as they model non-convex geometries with a high order of symmetry and are easy to construct.

The non-convexity of cross- and star-shaped particles increases with decreasing sphericity (ψ). Various definitions for sphericity have been proposed [38–40], whereby the most common definition is the ratio of the surface area of a sphere to the surface area of a non-spherical particle with the same volume as the sphere [39,41,42]. The present work uses this definition and thus for a sphere $\psi = 1$ and for non-convex particles $\psi < 1$. The sphericity of the particle shapes modeled in this work ranges from $\psi = 0.99$ to 0.42, hence covering a broad range of shapes from almost sphere-like to very slender highly non-convex shapes (Figure 3e). Other works [20,24] describe star-shaped particles by the particle aspect ratio (defined as the ratio of the overall length of a particle L to the diameter of the

protruding arms d_p (Figure 3)). The relationship between the particle aspect ratio and the particle sphericity is given in the appendix in Table 3.

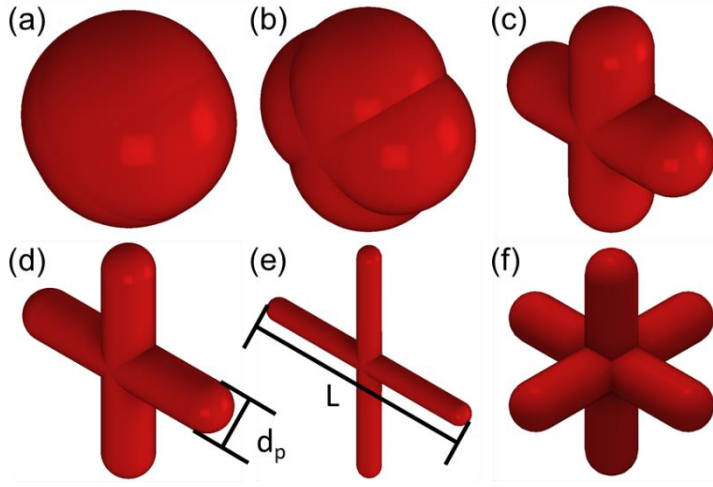


Figure 3: Selection of cross- and star-shaped particle geometries with varying sphericities (Ψ): a) Cross-shaped particle with $\Psi=0.99$, b) cross-shaped particle with $\Psi=0.96$, c) cross-shaped particle with $\Psi=0.75$, d) cross-shaped particle with $\Psi=0.59$, e) cross-shaped particle with $\Psi=0.47$ and f) star-shaped particle with $\Psi=0.53$.

Simulation domains

Four different domain configurations (defined by the confining walls) were assessed in this work: (i) 2D simulations in which cross-shaped particles cannot move in the z-direction (coordinate system shown in Figure 4). In these 2D simulations the domain width W_{dom} (x-direction) is equal to 30 times the particle length L . Therefore, W_{dom} changes with particle shape Ψ ; (ii) Pseudo-2D simulations in a cuboidal domain with a transverse thickness T (z-direction) equal to L . As in the 2D simulations, $W_{dom} = 30 \times L$; (iii) Pseudo-2D simulations in a cuboidal domain with $T = 2 \times L$ and $W_{dom} = 30 \times L$ and (iv) 3D simulations in a cylindrical domain of diameter $10 \times L$. A visualization of the pseudo-2D simulation with $T = 2 \times L$ is given in Figure 4a.

To initialize a simulation, the domain was filled by placing all of the particles on a regular lattice with a space of $1.5 \times d_p$ between each particle. The height of the simulation domain (y-direction) was chosen just large enough to accommodate all of the particles in the initialization lattice. The particles were initialized with a random rotational orientation and a random velocity v ($-0.25 \text{ m/s} < v < 0.25 \text{ m/s}$) in the y- and z-directions (2D and $T = L$ cases) or a random velocity in all three directions (3D and $T = 2 \times L$ cases). The particles were allowed to settle for a time $t_{settle} = 3 * \sqrt{2h/g}$, where g is the acceleration due to gravity. After time t_{settle} , the particles had come to rest as the average displacement of the particles per time-step approached numeric precision, h is the domain height. Once the particles had settled, the domain was compressed by moving a planar wall from the top downwards with a speed of 0.25 m/s until the packing exerted a force of 500 N onto the top wall. This procedure simulated the uniaxial compression of a granular material in a container with rigid walls.

The number of particles in each simulation N was such that the height of the packing (after compression) was at least twice as high as W_{dom} (or in the case of a cylindrical domain the diameter of the cylinder). In the different configurations N ranged from 1800 to 34500.

To avoid crystallization at low values of ψ , a particle size distribution, was introduced. In 2D simulations, the polydispersity factor (by which the particle size was scaled) was ± 0.3 for $\psi > 0.88$, and ± 0.15 for $0.88 \geq \psi > 0.75$. For pseudo-2D and 3D simulations, the polydispersity factor was ± 0.2 for $\psi > 0.86$. As reference cases, packings of spherical particles (diameter $d_p = 0.005$ m, polydispersity factor ± 0.2) in a 2D domain with $W_{dom} = 30 \times d_p$ and in a cylindrical domain with a cylinder diameter of $10 \times d_p$ were simulated.

Data analysis: Contact forces, stress analysis and packing structure

Previous studies using spherical particles typically focused on the normal component of the contact force [12–14]. Thus, we likewise report here the distribution of the normal contact forces. For the computation of the probability distribution of the contact forces, $P(f)$, the normalized forces f were sorted into 50 bins of size 0.2 (range 0-10).

Particle stresses were obtained by calculating first the stress tensor of the individual particles according to [43]:

$$\bar{\sigma} = \frac{1}{V} \begin{bmatrix} \sigma_{xx} & \sigma_{xy} & \sigma_{xz} \\ \sigma_{yx} & \sigma_{yy} & \sigma_{yz} \\ \sigma_{zx} & \sigma_{zy} & \sigma_{zz} \end{bmatrix} = \frac{1}{V} \sum_c \bar{F}_{n+t}^c \bar{r}^c \quad (3)$$

where V is the particle volume, c is the number of all particle contacts, \bar{F}_{n+t} is the sum of the normal contact force and the tangential contact force and \bar{r} is the vector pointing from the center of the particle to its contact point. The particle stress tensor was diagonalized to obtain the principal stresses. Additionally, this work reports the sum of the elements of the diagonalized stress matrix (trace) of each particle, i.e. the first stress invariant of the tensor for each particle ($I_{1,i}$). Similar to the presentation of the contact forces $I_{1,i}$ is normalized by its mean ($\langle I_1 \rangle = \frac{1}{N} \sum_i^N I_{1,i}$) yielding $i = I_{1,i}/\langle I_1 \rangle$.

The packing morphology was analyzed by calculating the radial distribution function (RDF) which is given by Eq. (4). The RDF can be interpreted as the number of particles that are located in a differential volume shell (thickness Δr) with a distance r from the particle center, divided by the expected number of particles [44].

$$G(r) = \frac{N_{RDF}(r)}{4\pi r^2 \Delta r N \rho} \quad (4)$$

Here ρ is the average number density of particles (number of particles in the simulation domain divided its volume) and N_{RDF} is the number of particles in the differential volume shell given by:

$$N_{RDF} = \sum_i^{N_{10L}} \sum_{j \neq i}^N \delta(r - r_{ij}) \quad (5)$$

where δ is the Dirac delta function, r_{ij} is the distance between the center of particle i to the center of particle j and N_{10L} is the number of particles which have a distance of at least $10 \times L$ from each side wall as well as the top and bottom of the 2D domain. This area is sketched in Figure 4b. In the 3D case, N_{10L} corresponds to the number of particles that have at least a distance of $10 \times L$ from the top and bottom wall and a distance of $3 \times L$ from the cylinder wall. We exclude particles close to the wall because these particles have no close neighbors outside of the walls.

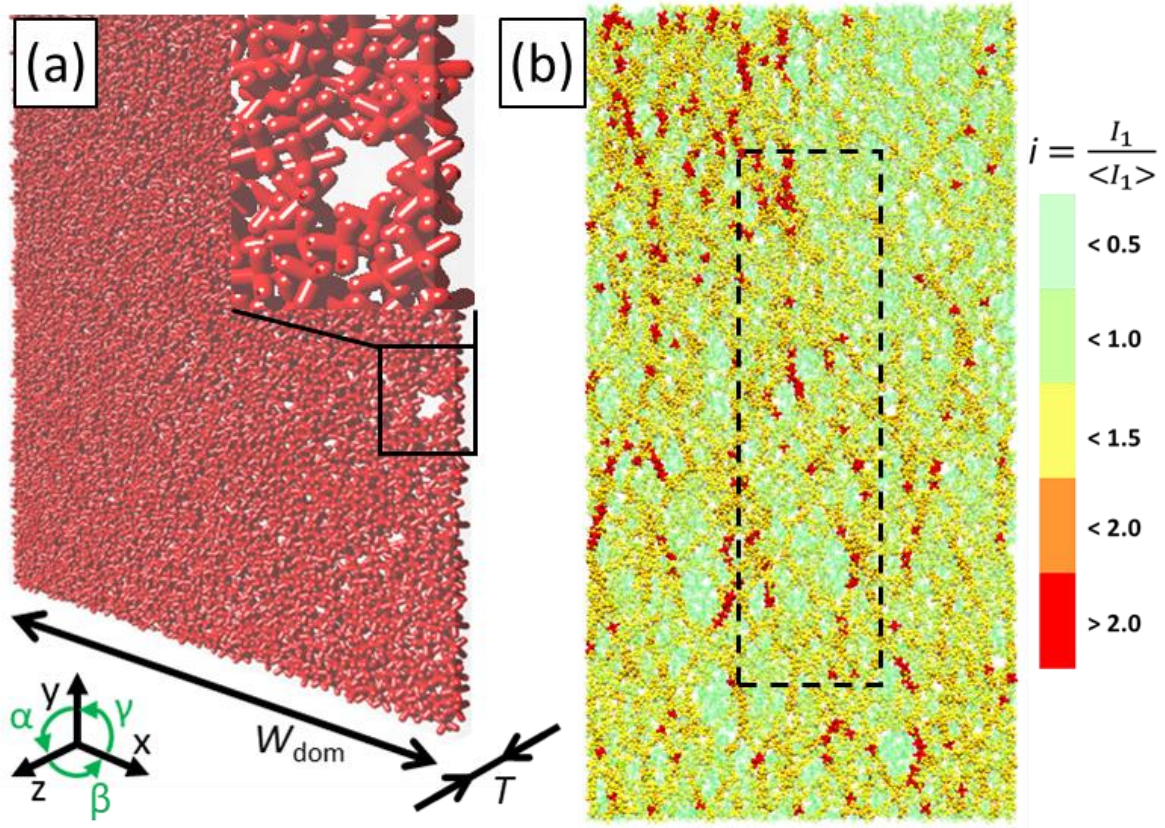


Figure 4: a) Visualization of a pseudo-2D packing of star-shaped particles ($\Psi = 0.619$) with $W_{\text{dom}} = 30 \times L$ and $T = L$ (L = particle length). b) Visualization of the normalized first stress invariant ($i = I_{1,i}/\langle I_1 \rangle$) of the packing shown in (a). The dashed area depicts the area which was used to calculate the radial distribution function (RDF). The results of the RDF are shown in Figure 7.

Results

Contact force distributions

As a first approach, we assess whether our simulations support a previously reported trend that the exponential tail of $P(f)$ becomes longer for increasingly non-spherical particles [13–15,25]. Currently, it is unclear whether such a trend is limited to a given domain dimensionality (2D vs 3D) and whether compressed packings show the same behavior as sheared systems. Figure 5 plots the probability distributions of the normal contact forces normalized by their mean, $P(f)$, for different particle sphericities and domain configurations.

For 2D domains, the $P(f)$ of crosses with the highest investigated sphericity ($\Psi = 0.995$) and spheres are very similar (Figure 5a). In 2D packings, changes in the $P(f)$ when transitioning from packings of spherical particles to slightly non-spherical particles seem to occur gradually. Figure 5a also plots the numerical expression for $P(f)$ as proposed by Mueth et al. [12]:

$$P(f) = a(1 - be^{-f^2})e^{-\beta f} \quad (6)$$

In this equation a , b and β are fitting parameters. Somewhat surprisingly, the empirical Eq. (6), although extracted originally from a packing of spheres agrees well with the data for low sphericity cross-shaped particles in 2D, but not with the simulation results of spheres. A possible reason for this deviation might be the fact that Mueth et al. [12] studied 3D packings and only recorded contact forces at the wall. Indeed, the numerical results of a packing of spheres in a 3D domain, Figure 5d, agree very well with Eq. (6).

When comparing the contact force distribution, $P(f)$, of cross-shaped particles (2D domain) as a function of their sphericity (Figure 5a), one can observe that the length of the exponential tail of $P(f)$ increases with decreasing ψ . However, the increase in the length of the exponential tail is limited. Even in packings of cross-shaped particles with a sphericity of $\psi = 0.473$ (lowest sphericity modeled) only four individual contact forces (out of 10^5) have a value of $f > 8$. The general type A shape of the distributions, i.e. a peak at $f \approx 1$ and an exponential tail is independent of particle sphericity when the packing is restricted to 2D. Hence, our results confirm the observations by Saint-Cyr et al. [14] who modeled trimers ($1 \geq \psi \geq 0.76$) and observed that the shape of $P(f)$ and the location of its peak is independent of particle sphericity in compressed 2D packings.

Turning now to pseudo-2D packings of star-shaped particles (Figure 5b and Figure 5c for, respectively, $T = L$ and $T = 2 \times L$), one observes a change in the shape of $P(f)$ from type A to type B with decreasing particle sphericity. Generally, the peak at $f \approx 1$ becomes less pronounced and the length of the exponential tail increases with decreasing sphericity. Only for particles with the highest sphericity ($\psi = 0.995$) the shape of $P(f)$ in pseudo-2D packings coincides with the shape that was observed in 2D simulations.

When increasing the transverse thickness of the pseudo-2D simulations ($T = 2 \times L$, Figure 5c) and ultimately reaching full 3D simulations, Figure 5d, the shape of $P(f)$ changes further, i.e. the peak of $P(f)$ remains at $f \approx 1$ for high-sphericity particles but is no longer visible for low-sphericity particles ($\psi = 0.461$ and $\psi = 0.419$). Furthermore, the length of the exponential tail increases significantly for $\psi < 0.7$ when increasing the transverse thickness of the domain to $T = 2 \times L$ and 3D. It has been suggested that type A distributions are essentially Gaussian-like (centered around $f \approx 1$, albeit truncated at $f = 0$) which would indicate that the forces are distributed homogeneously [13,45]. The similarity between a type A distribution and a Gaussian-shaped distribution is shown in Figure 1. One can see that a Gaussian is a good fit for type A distributions for $f < 3$, but the type A distribution has a longer tail. On the other hand, the lack of a peak at $f \approx 1$ and the long exponential tails of type B distributions represent a heterogeneous force distribution with a large number of below-average contact forces but also some contact forces that are ten times above average.

To summarize, our results show that in pseudo-2D and 3D packings the shape of $P(f)$ changes from type A to a type B when the particle sphericity decreases below the critical value $\psi_{\text{crit}} = 0.7$ (but not in 2D packings). The shape change comes with an increasing length of the exponential tail of $P(f)$ and a decreasing prominence of the peak at $f \approx 1$ with decreasing particle sphericity. Our results unify the observations of several previous studies: Saint-Cyr et al. [14] and Azéma and Radjai [15] who observed exclusively type A distributions in compressed 2D packings of non-spherical particles. On the other hand, Gan et al. [25] who simulated ellipsoids with $\psi \geq 0.7$ in 3D packings observed type A distributions and Murphy et al. [13] who simulated Z-shaped particles with $\psi = 0.45$ in 3D packings and observed type B distributions.

Combing the results of our simulations with previously reported observations allows us to draw the following general conclusion for the shape of $P(f)$ in 2D and 3D packings of compressed non-spherical particles with different shapes and sphericities:

- With decreasing particle sphericity, the contact force distribution of compressed 3D packings becomes more heterogeneous. This is evidenced by the increasing length of the exponential tail of the contact force distribution with decreasing particle sphericity for $\psi < \psi_{\text{crit}} = 0.7$, independent of the specific particle shape.
- In compressed 2D packings the length of the exponential tail of the contact force distributions does not depend on particle sphericity.

The heterogeneity of $P(f)$ needs to be considered when designing particles for specific applications such as aleatory construction for which non-convex particles with low sphericity (e.g. $\psi = 0.45$ [13]) are desired. Such particles need to be able to withstand the highest contact forces, that can reach values that are an order of magnitude higher than the mean contact force.

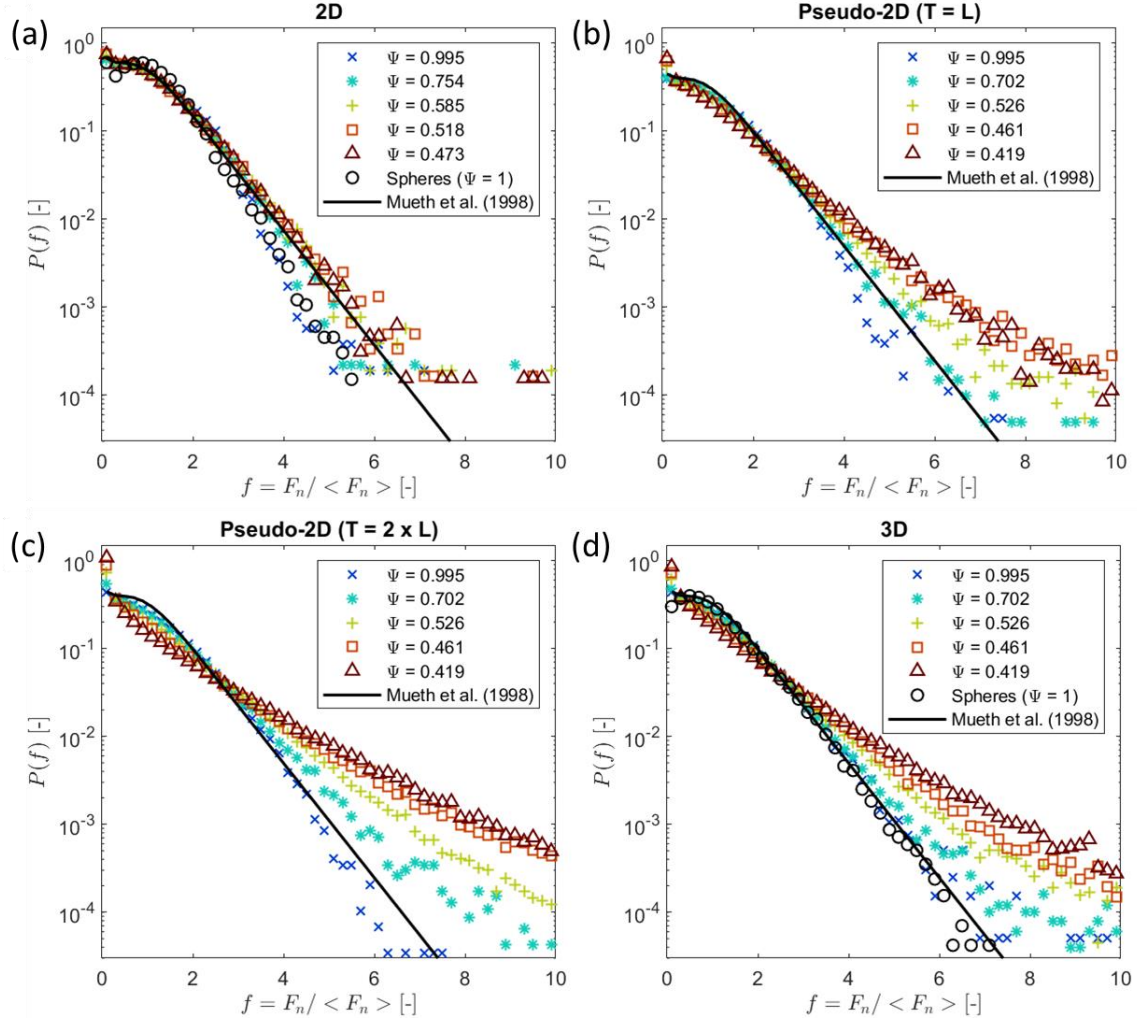


Figure 5: Probability distribution functions, $P(f)$, of the normal contact force (F_n) normalized by the mean normal contact force ($\langle F_n \rangle$) for all four packing domains simulated. For each packing configuration the full range of particle sphericities simulated is shown. For reference a 2D simulation of spheres is included in (a) and a 3D simulation of spheres is included in (d). Each panel also plots the probability distribution function predicted by the empirical equation (Eq. (6)) of Mueth et al. [12], which was derived from compressed 3D packings of glass spheres.

Quantification of the length of the exponential tail

Next, a quantitative description of the length of the exponential tail is explored. Currently, there is no agreement on the mathematical function that describes best the probability distribution of the contact forces, $P(f)$. While some have argued that $P(f)$ in a packing of spheres such as the one shown in Figure 5a, can be fitted best by a Gaussian distribution [13,45], Mueth et al. [12] proposed Eq. (6) since a saddle point rather than a peak (at $f \approx 1$) was observed. However, as already shown in Figure 1, neither a Gaussian function nor Eq. (6) describe the force distribution in 3D packings of low sphericity particles (type B shape). Nonetheless, it is generally agreed that for $f > 1$, $P(f)$ decays exponentially, independent of the domain dimension and particle sphericity. This observation motivated Azéma and Radjai [15] to propose the following fit to the tail ($f > 1$) of $P(f)$:

$$P(f) = e^{-kf}, \quad f > 1 \quad (7)$$

Here the exponent k is a fitting parameter that will be used to quantify the length of the exponential tail of $P(f)$. In the following, we will focus on the region $f > 1$ of $P(f)$, due to the importance of the large forces which can potentially lead to the fracture of particles and endanger a stable packing.

Figure 6a plots the exponent k as a function of particle sphericity. The exponent k was obtained by fitting the exponential tail ($f > 1$) of the different $P(f)$ (Figure 5) with Eq. (7). Error bars are omitted in Figure 6a for clarity (the 95% confidence bounds for k are typically within ± 0.025). Qualitatively the homogeneity of $P(f)$ decreases as the length of the tail increases (i.e. a lower value of k).

For particles of high sphericity ($\psi = 0.995$), the values obtained for k are in the range $1.28 \geq k \geq 1.47$. These values are in between the values obtained by Mueth et al. [12] (packings of glass spheres in 3D with $k = 1.5$) and Gan et al. [25] (3D packing of spheres with $k = 1.24$).

Turning now to less spherical particles: In 2D packings, k decreases slightly with decreasing ψ , i.e. $k = 1.42$ for $\psi = 0.995$ and $k = 1.32$ for $\psi = 0.47$. In 2D packing the decrease of k with decreasing ψ can be fitted well by a linear function (dashed black line in Figure 6a). The comparatively high value of $k = 1.32$ for the lowest sphericity values studied ($\psi = 0.47$) shows that there are relatively few cases of high contact forces in 2D packing of low sphericity particles. Good agreement is also seen when including data for k obtained by other works that have assessed compressed 2D packings (e.g. the data of Saint-Cyr et al. [14] is for trimer particles).

In pseudo-2D and 3D packings $k = 1.38 \pm 0.14$ for $\psi > \psi_{\text{crit}} = 0.7$. For $\psi < \psi_{\text{crit}}$ k decreases exponentially with decreasing ψ and reaches a value of $k = 0.87 \pm 0.13$ for the lowest sphericity investigated, i.e. $\psi = 0.42$. An exponential fit of k in pseudo-2D ($T = 2 \times L$) packings is shown by a solid line in Figure 6a. Hence, for $\psi < \psi_{\text{crit}}$ the probability of finding large contact forces ($f > 8$) increases exponentially and the contact force distributions become increasingly heterogeneous. The critical sphericity value, i.e. $\psi_{\text{crit}} = 0.75$ for crosses (2D) and $\psi_{\text{crit}} = 0.7$ for stars (3D) is the lowest sphericity for which a contact between two particles always involves the hemispherically-capped ends of the particles. This can be explained by the fact that, at this critical sphericity the arms protruding from a particle are exactly twice as long as the particle radius (Figure 6c). For $\psi > \psi_{\text{crit}}$, contacts will always involve the end-caps of a particle (Figure 6b), while for $\psi < \psi_{\text{crit}}$, contacts can also involve the flat/cylindrical section of the protruding arms (Figure 6c). Particles that only contact each other with the hemispherical end-caps, i.e. star-shaped particles with $\psi \geq 0.7$, are more likely to slip relative to each other when a load is applied. Conversely, particles with contacts that involve the flat/cylindrical sections of the arms, i.e. star-shaped particles with $\psi < 0.7$, are less likely to slip relative to each other which means that they are more likely to jam. When a particle jams during compression, the contact forces acting on such a particle can increase substantially (and without the particle unjamming the contact forces cannot relax). These high contact forces give rise to the long exponential tail of $P(f)$ for low sphericity particles, in particular for star-shaped particles with $\psi < 0.7$. Whereas this rationale explains the transition at $\psi_{\text{crit}} = 0.7$ for pseudo-2D and 3D packings, it is unclear why such a pronounced transition is absent for 2D packings. We speculate that the reason might lie in the particular spatial distribution (morphology) of the particles which will be investigated in the following.

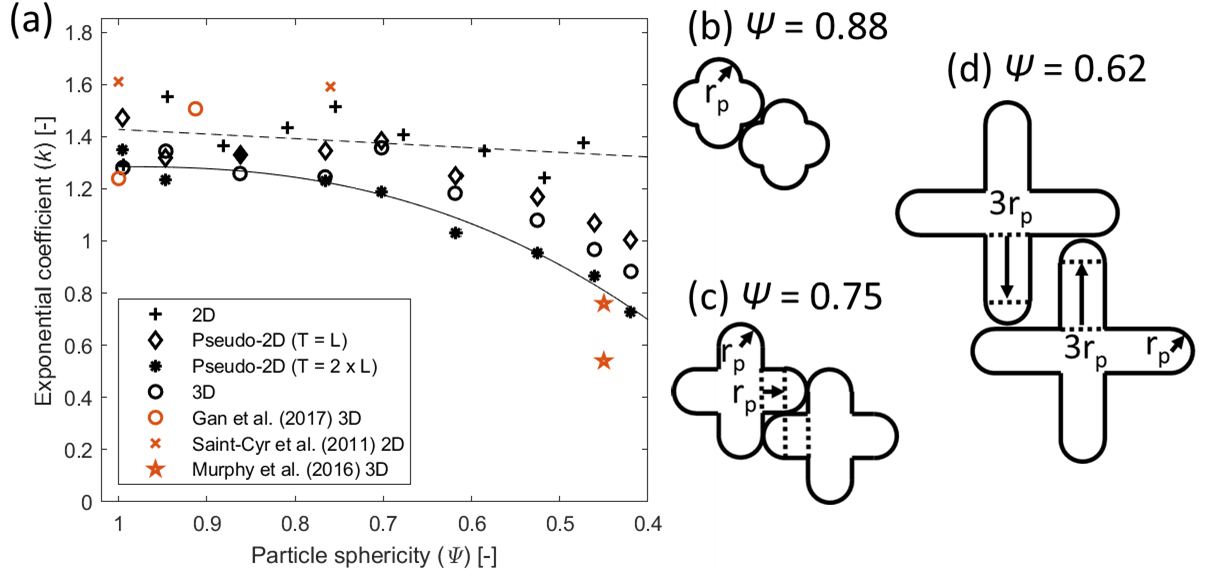


Figure 6: (a) Exponent k (Eq. (7)) obtained by fitting the exponential tail ($f > 1$) of the contact force distributions. Results of the present work are shown by black markers, while red markers denote results from previously published studies. The dashed line is a linear fit ($k(\psi) = 0.18(1-\psi)+1.43$) to the values of k obtained in 2D packings (+), while the solid line is an exponential fit ($k(\psi) = -2.03(1-\psi)^{2.43}+1.29$) to the values of k obtained in pseudo-2D ($T = 2 \times L$) packings (*). b)-d) Sketches of cross-shaped particles showing how the length of the protruding arms change with sphericity.

Packing morphology

By analyzing the probability distribution of the contact forces, $P(f)$, we found that in compressed pseudo-2D and 3D particle packings the length of the exponential tail of $P(f)$ increases with decreasing particle sphericity. In contrast, in 2D packings, the length of the exponential tail of $P(f)$ does not depend strongly on the particle sphericity. Hence, the question why the behavior of 3D packings differs distinctively from 2D packings remains unanswered. This behavior cannot be explained by differences in the solid fraction, as the solid fraction versus particle sphericity does not show clear differences between 2D and 3D packings (appendix Figure 9).

Instead of assessing the structure of a packing by an averaged, global parameter, such as the solid fraction, the morphology of the packings was assessed by calculating their radial distribution functions, RDF ($G(r)$, Figure 7). The RDF gives the average number of particles that are found at a distance r from a particle center divided by the average number of particles expected based on the particle number density of the whole packing. Here we have considered the center of mass of a cross or star-shaped particle as the particle center. In the RDF plots, the r -axis is normalized by the respective particle length L .

Comparing the RDFs in 2D packings as a function of sphericity (Figure 7a), one observes that for cross-shaped particles of low sphericity ($\psi = 0.75$) the first ($r/L = 0.76$) and second ($r/L = 1.5$) peak, are more prominent compared to the first ($r/L = 1$) and second ($r/L = 1.91$) peak of more spherical particles ($\psi = 0.995$). These peaks correspond to particle configurations of local crystallinity which are also the closest possible arrangements of interlocking particles. Sketches of such crystalline particle configurations are shown in Figure 7 (and enhanced in the appendix in Figure 10). More pronounced peaks imply a more frequent occurrence of the respective particle configurations. The distances D_1 , D_2 , D_3 between the centers of two interlocking particles, as defined in Figure 7, can be calculated by:

$$D_1 = \sqrt{d_p^2 + [(L + d_p)/2]^2}, \quad D_2 = 2D_1, \quad D_3 = 3D_1 \quad (8)$$

For cross-shaped particles with $\psi = 0.75$ the values of the first ($r/L = 0.76$) and second ($r/L = 1.5$) peak of the RDF are close to the geometrically determined values of the D_1 and D_2 configurations ($D_1/L = 0.75$ and $D_2/L = 1.49$). This indicates that the peaks in the RDF indeed correspond to the proposed closest crystalline configurations. In the RDF of 2D packings of particles with $\psi = 0.75$ the peak positions are shifted to lower values of r/L compared to the RDF of 2D packings of more spherical particles ($\psi = 0.995$). The position of the peaks (D_1/L) shifts to lower values for decreasing ψ because L increases with decreasing ψ and $\frac{D_1}{L} \propto \frac{(L+\sqrt{L})}{2L} < 1$. For 2D packings of cross-shaped particles with $\psi = 0.75$ a small third peak can be seen at $r/L = 2.23$, which corresponds to a similar packing configuration as the one described above (four-particle configuration) with an analytical value of $D_3/L = 2.24$. These first three peaks can also be seen in the RDFs of 2D packings of particles with lower sphericity. The positions of the peaks as well as the analytically obtained positions are shown in Table 2. Since these three peaks are observed even in 2D packings of highly non-spherical particles one can conclude that structures of local crystallinity can be observed in all of these packings.

Table 2: Peak positions observed in the RDFs of 2D packings of cross-shaped particles and peak positions calculated according to Eq. (8).

ψ	1 ST PEAK	D_1/L	2 ND PEAK	D_2/L	3 RD PEAK	D_3/L
0.473	0.55	0.55	1.12	1.11	1.66	1.66
0.518	0.58	0.57	1.14	1.14	1.73	1.71
0.585	0.62	0.61	1.25	1.21	1.82	1.82
0.754	0.76	0.75	1.50	1.49	2.23	2.24
0.995	1.00	0.98	1.91	1.95	none	2.93

Figure 7b plots the RDFs of star-shaped particles in 3D packings. The RDF of particles with $\psi = 0.995$ shows a first peak at $r/L = 1$ and a second peak at $r/L = 1.9$. These peaks are at the same positions as in the RDF of 2D packings of cross-shaped particles with $\psi = 0.995$ because both particle types are almost spherical and cannot interlock. In 3D packings of star-shaped particles with $\psi = 0.702$ the first peak is located at $r/L = 0.7$ and the second peak at $r/L = 1.37$. Compared to 2D packings of cross-shaped particles with similar sphericity, the peaks are shifted to lower r/L values. This observation can be explained by the fact that star-shaped particles in 3D packings have additional degrees of freedom compared to cross-shaped particles in 2D packings allowing closer packing configurations in 3D packings. A sketch of the closest packing of star-shaped particles in 3D is shown in Figure 7b (enlarged sketch in the appendix, Figure 10). The closest distance (J_1) between the centers of two star-shaped particles in the packing configuration shown in Figure 7b is:

$$J_1 = \sqrt{3}d_p \quad (9)$$

Hence, in 3D packings of star-shaped particles with $\psi = 0.702$, the first peak J_1 is expected at $r/L = 0.58$ and the second peak at $r/L = 1.15$. However, the first and second peak are found at $r/L = 0.7$ and $r/L = 1.37$, respectively. This result indicates that the most likely packing configuration of star-shaped particles in a compressed 3D packing is considerably looser than the closest possible crystalline packing configuration. Hence, 3D packings have a different morphology to 2D packings, as the peak location in the RDF of 2D packings of cross-shaped particles agrees very well with the closest possible crystalline packing configuration which, however, is not the case for 3D packings.

Additionally, when comparing the RDF of 2D and 3D packings, one finds that the height of the peaks in the RDF of 3D packings is lower than in 2D packings, a further sign of a reduced crystallinity when introducing an additional dimension. The reduced peak height is particularly noticeable when

comparing the RDF of cross-shaped particles with $\psi = 0.754$ (2D packing, Figure 7a) with the RDF of star-shaped particles with $\psi = 0.702$ (3D packings, Figure 7b). Even a third peak is visible in the RDF of the 2D packing ($\psi = 0.754$), whereas a third peak is absent in the RDF of a 3D packing ($\psi = 0.754$). The reduced crystallinity in 3D packings is even more pronounced for particles of lower sphericity, i.e. $\psi < 0.702$ ($\psi < \psi_{\text{crit}}$), in which even the first peak in the RDF disappears completely, indicating an amorphous packing structure.

To summarize, the crystallinity of 3D packings of star-shaped particles decreases with decreasing particle sphericity. In 2D packings of cross-shaped particles, however, such a decrease in crystallinity with decreasing sphericity could not be observed. The data in Figure 7 shows that interlocked, crystalline, configurations are found in 2D packings of cross-shaped particles with $\psi < 0.7$, whereas such configurations do not seem to be present to a large extent in 3D packings of star-shaped particles with $\psi < 0.7$. This can be explained by considering that 3D star-shaped particles have three additional degrees of freedom (one translational degree and two rotational), compared to 2D cross-shaped particles. It is therefore less likely that star-shaped particles, when dropped into a 3D container followed by compression will configure themselves into a highly crystalline packing.

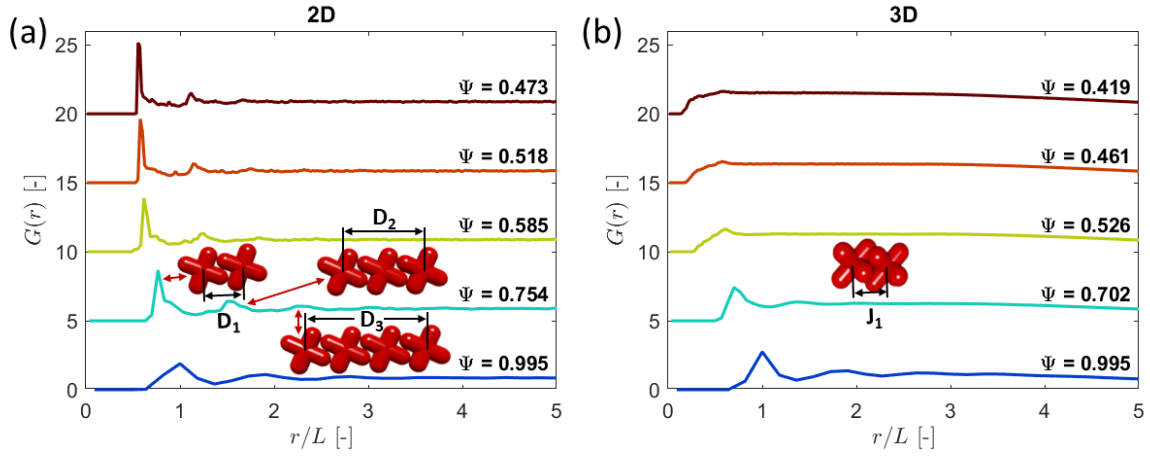


Figure 7: Radial distribution function (RDF), $G(r)$, for (a) 2D and (b) 3D packings of particles of different sphericity. For better readability, the curves are shifted vertically with an offset of 5. In 2D packings, the distance between the particle centers corresponding to the first, second and third peak are labeled D_1 , D_2 and D_3 , while in 3D packings J_1 labels the shortest possible distance between particle centers. The distances D_{1-3} can be determined analytically according to Eq. (8), and J_1 according to Eq. (9).

Linking force distributions to packing morphology

We described above that in 3D packings, below a critical value of $\psi < \psi_{\text{crit}} = 0.7$, the length of the exponential tail of the contact force distribution increases with decreasing particle sphericity. The increasing length of the exponential tail in 3D packings (and not in 2D packings) for sphericities $\psi < 0.702$ seems to coincide with the disappearance of peaks in the RDF. To understand this observation, we revisit the work by Luding [17], who used the DEM to investigate particle stresses of monodisperse and polydisperse packings of discs in a perfectly hexagonal 2D lattice. For perfectly monodisperse particles, a uniform particle stress distribution was observed. However, as soon as some polydispersity was introduced, by varying the disc diameter by a small amount ($\pm 0.33\%$), localized force chains were observed in the particle packing. Luding [17] also observed that the probability of large particle stresses to occur increases with increasing polydispersity, i.e. the length of the exponential tail of the particle stress distribution increases with increasing polydispersity. One can interpret the findings of the present work as a generalization of Luding's [17] results to non-spherical particles, i.e. a decreasing crystallinity of the packing (induced by either polydispersity or non-sphericity) leads to wider, less homogeneous, contact force and particle stress distributions, provided that the following two assumptions hold: (1) The introduction of polydispersity does lead to a reduction in crystallinity and

(2) the behavior of the particle stress distribution, $P(i)$, depending on particle sphericity is very similar to that of the contact force distributions, $P(f)$.

Concerning the first assumption, there is indeed evidence of reduced peak heights in the RDF of a hexagonal packing with 5% polydispersity, when compared to the RDF of a monodisperse packing [46]. The reduced peak height hints towards a reduced crystallinity in polydisperse packings, however, further research is required to confirm the assumption.

To confirm the second assumption, that the exponential decay of the particle stress distribution is similar to the decay of the contact force distribution, one can compare $P(f)$ and $P(i)$, i.e. the probability distribution of the normalized first stress invariant $i = I_{1,i}/\langle I_1 \rangle$ shown in Figure 8. Generally, the shape of $P(i)$ is similar to the shape of $P(f)$, i.e. for 2D packings distributions of type A and for 3D packings of low sphericity particles distributions of type B are obtained. For high sphericity ($\psi > 0.7$) cross-shaped particles in 2D packings (Figure 8a), the distributions exhibit a pronounced peak at $i = 1$, which disappears for $\psi < \psi_{\text{crit}} = 0.7$ as $\lim_{i \rightarrow 0} P(i)$ increases with decreasing ψ . Specifically, in 3D packings of star-shaped particles, $P(i)$ has a type A-like distribution for $\psi \geq 0.7$ (peak at $i = 1$ and an exponential tail of similar length as in 2D packings), and no particle experiences a stress invariant with a magnitude of more than 6 times the mean. However, for 3D-packings of star-shaped particles with $\psi < \psi_{\text{crit}}$, the shape of $P(i)$ changes to a type B distribution and the length of the exponential tail of $P(i)$ increases with decreasing particle sphericity. The steep increase of $\lim_{i \rightarrow 0} P(i)$ implies that there is an increasing number of particles that experience only a very small fraction of the load that is put on the packing by uniaxial compression. At the same time, owing to the increasing length of the exponential tail, some particles experience stresses that are significantly higher than the mean. These trends match the behavior of $P(f)$, as described further above.

The transition of $P(i)$ to a type B distribution in 3D packings of star-shaped particles for decreasing sphericity, is attributed to an increasing frequency of contacts between the flat parts of the arms protruding from the particles (Figure 6c). Such contacts are only possible for star-shaped particles with $\psi < \psi_{\text{crit}}$, whereas for $\psi \geq \psi_{\text{crit}}$ all contacts between star-shaped particles involve the hemispherical end-caps of the spherocylinders. Particles forming contacts between the flat parts of the spherocylinders are less likely to rearrange during uniaxial compression. This effect can also be interpreted as an increased apparent friction coefficient between particles. Such particles are more likely to jam during uniaxial compression, instead of rearranging into a configuration which would reduce the stress acting on the particle. As a consequence, high stresses can build up which results in an increased length of the tail of $P(i)$. The build-up of stresses in some particles leaves other particles to contribute little to the stress transmission in the packing leading in turn to an increase of $\lim_{i \rightarrow 0} P(i)$ with increasing apparent friction [47].

To summarize, the dependence of the length of the exponential tail of $P(i)$ on particle sphericity is very similar to the respective behavior of $P(f)$. Hence, our results can indeed be considered as a generalization of Luding's [17] observation of the effect of polydispersity on the stress distribution in particle packings, i.e. a decreasing crystallinity (due to increasing non-sphericity or polydispersity) leads to a extended tail of the contact force and particle stress distributions.

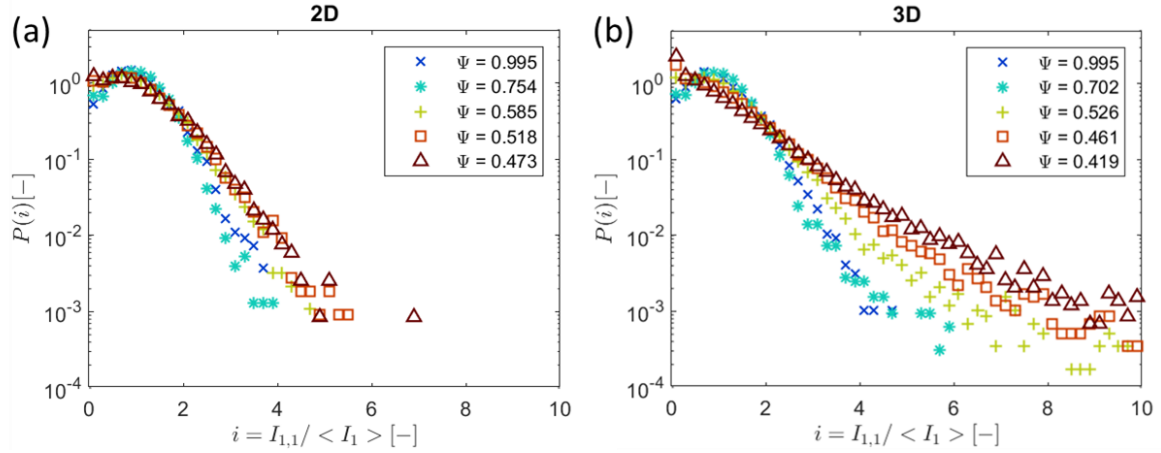


Figure 8: Probability distributions of the normalized first stress invariants $P(i)$ as a function of particle sphericity in (a) 2D and (b) 3D packings. The normalized first stress invariants i are obtained by normalizing the first stress invariants $I_{1,i}$ by $\langle I_1 \rangle$.

Conclusions

This work investigated compressed 2D and 3D packings of non-spherical, non-convex, cross- and star-shaped particles using the DEM. Such non-convex particles can interlock forming packings that may sustain compressive and tensile forces despite containing purely non-cohesive particles. The particle sphericity (ψ) was varied in the range $\psi = 0.42 - 1$. The morphology of the packings was investigated by calculating the radial distribution function (RDF). Through the RDF we have established a link between the packing morphologies and the contact force probability distributions as expressed by the decay exponent k .

In 2D packings of cross-shaped particles a linear decrease of k was observed, from $k = 1.42$ for $\psi = 0.995$ to $k = 1.32$ for $\psi = 0.47$. For pseudo-2D and 3D packings of star-shaped particles k is independent of the sphericity ($k = 1.38 \pm 0.14$) for $\psi \geq 0.7$; however, for smaller sphericities (i.e. $\psi < 0.7$) the magnitude of k decreases exponentially with decreasing ψ . These findings connect for the first time the results of previous works [13,14,25] on compressed packings of non-spherical particles allowing us to draw the following general conclusions:

- In compressed 3D packings, the distribution of contact forces becomes more heterogeneous, i.e. the length of the exponential tail increases with decreasing particle sphericity, independent of particle type.
- In 2D packings the influence of the particle sphericity on the contact force distribution is minor.

We link the increasing heterogeneity of the distribution of the contact forces to the packing morphology, by showing that the increasing heterogeneity in the contact force distribution with decreasing sphericity is due to a decreased crystallinity in such packings. The link between a decreasing packing crystallinity and a more heterogeneous contact force distributions has been postulated previously by Luding [17], when assessing the effect of polydispersity on the homogeneity of the particle stress distributions. Hence, our results can be interpreted as a generalization of this previous observation providing further evidence that a reduced packing crystallinity, through either an increase of domain dimension, particle non-sphericity or polydispersity, leads to a more heterogeneous stress distribution.

Acknowledgments

This work has been financed by the Swiss National Science Foundation grant No. 200021_157122/1.

Appendix

Particles of low sphericity form packings with a low solid fraction. Figure 9 plots the solid fraction of a packing as a function of ψ and domain geometry. For 2D packings, we show the area fraction occupied by particles as well as the volume fraction, assuming that the domain has a transverse thickness that is equal to the particle diameter ($T = d_p$).

For a packing of non-spherical particles ($\psi > 0.9$), one observes an increase in solid fraction with decreasing sphericity, with a peak at $\psi = 0.9 - 0.95$. At this sphericity value, the particle shapes are the closest to a cuboidal shape. Cuboids can be stacked without any gaps. Reducing the sphericity further ($\psi \leq 0.9$), the particles become increasingly concave with an increased tendency to interlock, which leads to a decreasing solid fraction of the packing. The shape of the solid fraction versus sphericity curves is similar to the trends that have been observed previously simple spherocylinders and ellipsoids [48–50].

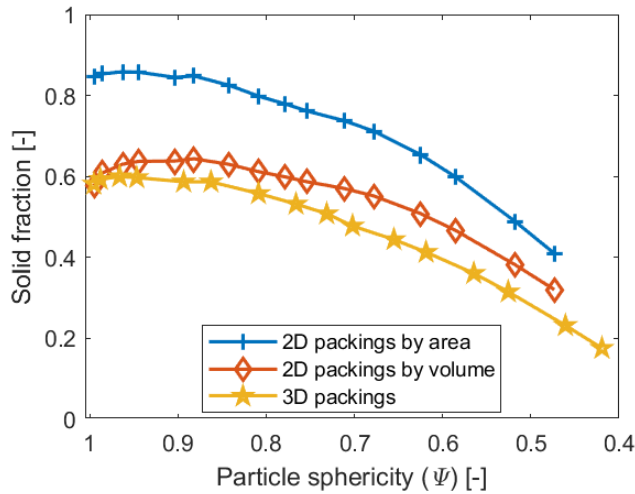


Figure 9: The solid fraction of packings as a function of sphericity and domain geometry.

The peaks in the RDF (Figure 7) result from specific particle configurations in which particles have the shortest possible distance between adjacent particle centers. Figure 10 visualizes such particle packing configurations for cross-shaped (RDF, Figure 7a) and star-shaped particles (RDF, Figure 7b).

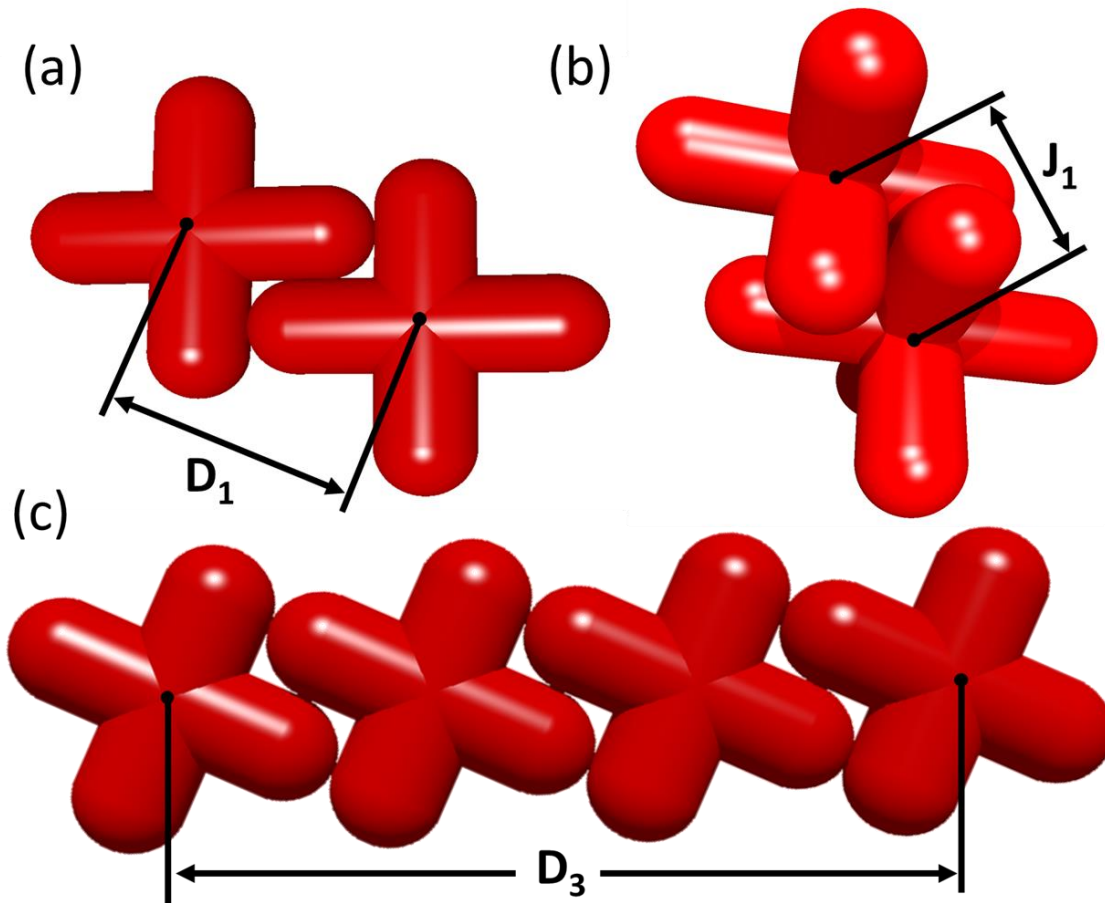


Figure 10: Visualization of particle configurations with the shortest possible distance (D_1 , D_3 , J_1) between particle centers (black dots): (a) cross-shaped particles used in 2D simulations, (b) star-shaped particles used in pseudo-2D and 3D simulations and (c) configuration of four cross-shaped particles. D_1 and D_3 can be calculated according to equation Eq. (8), and J_1 according to Eq. (9).

In this work, the particle shapes are identified by the particle sphericity, while some other works identify particles of the same star-shape by the aspect ratio, which is defined as the overall length of a particle (L) and the diameter of the protruding arms (d_p) (Figure 3) [20,24]. To aid the comparison to other works, Table 3 shows the relationship between the particle aspect ratio and particle sphericity.

Table 3: Relationship between the particle aspect ratio and the particle sphericity. The particle aspect ratio is defined as the overall length of a particle (L) and the diameter of the protruding arms (d_p).

Particle aspect ratio (L/d_p)	Sphericity cross-shape (2D)	Sphericity star-shape (3D)
1.1	0.995	0.995
1.7	0.933	0.933
2.25	0.842	0.809
3	0.754	0.702
4	0.677	0.619
6	0.585	0.526
8.5	0.518	0.462
11	0.473	0.419

Literature

- [1] B. Indraratna, D. Ionescu, and H. D. Christie, *J. Geotech. Geoenvironmental Eng.* **124**, 439 (1998).
- [2] L. D. Poulikakos and M. N. Partl, *J. Microsc.* **240**, 145 (2010).
- [3] N. Kaliyan, R. V. Morey, and D. R. Schmidt, *Biomass and Bioenergy* **55**, 322 (2013).
- [4] R. Linemann, J. Runge, M. Sommerfeld, and U. Weißgüttel, *Part. Part. Syst. Charact.* **21**, 261 (2004).
- [5] C. -h. Liu, S. R. Nagel, D. A. Schecter, S. N. Coppersmith, S. Majumdar, O. Narayan, and T. A. Witten, *Science* **269**, 513 (1995).
- [6] T. S. Majmudar and R. P. Behringer, *Nature* **435**, 1079 (2005).
- [7] A. Drescher and G. de Josselin de Jong, *J. Mech. Phys. Solids* **20**, 337 (1972).
- [8] R. C. Hidalgo, C. U. Grosse, F. Kun, H. W. Reinhardt, and H. J. Herrmann, *Phys. Rev. Lett.* **89**, 205501 (2002).
- [9] A. Rechenmacher, S. Abedi, and O. Chupin, *Geotech. London* **60**, 343 (2010).
- [10] M. Oda and H. Kazama, *Géotechnique* **48**, 465 (1998).
- [11] H. Laubie, F. Radjai, R. Pellenq, and F.-J. Ulm, *Phys. Rev. Lett.* **119**, 1 (2017).
- [12] D. M. Mueth, H. M. Jaeger, and S. R. Nagel, *Phys. Rev. E* **57**, 3164 (1998).
- [13] K. A. Murphy, N. Reiser, D. Choksy, C. E. Singer, and H. M. Jaeger, *Granul. Matter* **18**, 26 (2016).
- [14] B. Saint-Cyr, J.-Y. Delenne, C. Voivret, F. Radjai, and P. Sornay, *Phys. Rev. E* **84**, 041302 (2011).
- [15] E. Azéma and F. Radjaï, *Phys. Rev. E* **85**, 031303 (2012).
- [16] A. Abed Zadeh, J. Barés, T. A. Brzinski, K. E. Daniels, J. Dijksman, N. Docquier, H. O. Everitt, J. E. Kollmer, O. Lantsoght, D. Wang, M. Workamp, Y. Zhao, and H. Zheng, *Granul. Matter* **21**, 1 (2019).
- [17] S. Luding, *Phys. Rev. E - Stat. Physics, Plasmas, Fluids, Relat. Interdiscip. Top.* **55**, 4720 (1997).
- [18] E. Olsson, D. Jelagin, and M. N. Partl, *Road Mater. Pavement Des.* **20**, S604 (2019).
- [19] P. A. Cundall and O. D. L. Strack, *Geotechnique* **29**, 47 (1979).
- [20] Y. Zhao, J. Barés, and J. E. S. Socolar, *Phys. Rev. E* **101**, 062903 (2020).
- [21] K. Dierichs and A. Menges, *Granul. Matter* **18**, 25 (2016).
- [22] K. Murphy, L. Roth, D. Peterman, and H. Jaeger, *Archit. Des.* **87**, 74 (2017).
- [23] P. Aejmelaesus-Lindström, J. Willmann, S. Tibbits, F. Gramazio, and M. Kohler, *Granul. Matter* **18**, 28 (2016).
- [24] Y. Zhao, K. Liu, M. Zheng, J. Barés, K. Dierichs, A. Menges, and R. P. Behringer, *Granul. Matter* **18**, 24 (2016).
- [25] J. Q. Gan, Z. Y. Zhou, and A. B. Yu, *Powder Technol.* **320**, 610 (2017).
- [26] G. Lu, J. R. R. Third, and C. R. R. Müller, *Chem. Eng. Sci.* **127**, 425 (2015).
- [27] H. P. Zhu, Z. Y. Zhou, R. Y. Yang, and A. B. Yu, *Chem. Eng. Sci.* **62**, 3378 (2007).

- [28] Y. Guo, C. Wassgren, W. Ketterhagen, B. Hancock, and J. Curtis, Powder Technol. **228**, 193 (2012).
- [29] G. Lu, J. R. Third, and C. R. Müller, Granul. Matter **16**, 107 (2014).
- [30] G. Lu, R. C. Hidalgo, J. R. Third, and C. R. Müller, Granul. Matter **18**, 34 (2016).
- [31] G. Lu and C. R. Müller, Granul. Matter **22**, 50 (2020).
- [32] Vladimir J. Lumelsky, Inf. Process. Lett. **21**, 55 (1985).
- [33] M. J. Jiang, J. M. Konrad, and S. Leroueil, Comput. Geotech. **30**, 579 (2003).
- [34] M. Kodam, R. Bharadwaj, J. Curtis, B. Hancock, and C. Wassgren, Chem. Eng. Sci. **64**, 3466 (2009).
- [35] D. Höhner, S. Wirtz, H. Kruggel-Emden, and V. Scherer, Powder Technol. **208**, 643 (2011).
- [36] T. Kidokoro, R. Arai, and M. Saeki, Granul. Matter **17**, 743 (2015).
- [37] R. Kumar, A. Sarkar, W. Ketterhagen, B. Hancock, J. Curtis, and C. Wassgren, AIChE J. **64**, 1986 (2018).
- [38] L. Meng, C. Wang, and X. Yao, Phys. A Stat. Mech. Its Appl. **490**, 212 (2018).
- [39] I. Malinouskaya, V. V. Mourzenko, J.-F. Thovert, and P. M. Adler, Phys. Rev. E **80**, 011304 (2009).
- [40] Y. Yang, J. F. Wang, and Y. M. Cheng, Particuology **25**, 23 (2016).
- [41] A. Wachs, L. Girolami, G. Vinay, and G. Ferrer, Powder Technol. **224**, 374 (2012).
- [42] F. Ludewig and N. Vandewalle, Phys. Rev. E **85**, 051307 (2012).
- [43] R. J. Bathurst and L. Rothenburg, J. Appl. Mech. Trans. ASME **55**, 17 (1988).
- [44] J. D. Bernal, *The Bakerian Lecture, 1962. The Structure of Liquids* (1964).
- [45] J. Jose, A. van Blaaderen, A. Imhof, and A. Imhof, Phys. Rev. E **93**, 062901 (2016).
- [46] S. E. Phan, W. B. Russel, J. Zhu, and P. M. Chaikin, J. Chem. Phys. **108**, 9789 (1998).
- [47] N. Estrada, A. Taboada, and F. Radjaï, Phys. Rev. E - Stat. Nonlinear, Soft Matter Phys. **78**, 1 (2008).
- [48] A. Donev, I. Cisse, D. Sachs, E. A. Variano, F. H. Stillinger, R. Connelly, S. Torquato, and P. M. Chaikin, Science **303**, 990 (2004).
- [49] T. Marschall and S. Teitel, Phys. Rev. E **97**, 012905 (2018).
- [50] J. Zhao, S. Li, R. Zou, and A. Yu, Soft Matter **8**, 1003 (2012).